



# Grain Structure Prediction for Directionally Solidified Superalloy Castings

A. DURGA,<sup>1,2</sup> HUIJUAN DAI,<sup>3,4</sup> SHENYAN HUANG,<sup>3</sup> IAN SPINELLI,<sup>3</sup>  
and LANG YUAN<sup>3,5,6</sup>

1.—John F. Welch Technology Centre, GE Research, Bengaluru 560 066, India. 2.—Department of Materials Science and Engineering, KTH Royal Institute of Technology, Brinellvägen 23, Stockholm, Sweden. 3.—GE Research, Niskayuna, NY 12309, USA. 4.—GE Renewable, Greenville, SC 29615, USA. 5.—Department of Mechanical Engineering, University of South Carolina, Columbia, SC 29201, USA. 6.—e-mail: LANGYUAN@cec.sc.edu

A highly parallelized mesoscale solidification model based on a cellular automaton method was coupled with a macroscale process model to predict grain structure during directional solidification. The macroscale thermal model and a nucleation parameter (maximum nucleation density) for René N500 were verified and calibrated using temperature profiles obtained via thermocouples in step-geometry castings and grain structures analyzed by electron backscatter diffraction (EBSD), respectively. The calibrated model was then applied to a laboratory-scale turbine blade to predict its grain structures. The predicted grain sizes agreed with experimental measurements under different casting conditions. The established bulk nucleation parameter based on the simple geometry can be directly transferred to complex geometries. Grain calculations without accurate estimations of nucleation on the chill plate can still provide reasonably good predictions. Overall, a viable path to calibrate model inputs for grain structure models based on simple geometry, where faster iterations can be achieved, is demonstrated.

## INTRODUCTION

Grain structure control in castings, particularly in directionally solidified industrial gas turbine (IGT) blades made of Ni-based superalloys, is critical to obtain high-temperature strength and creep resistance.<sup>1</sup> Numerical modeling of the grain structure has been performed for various components made of directionally solidified Ni-based superalloys, e.g., slab, grain selectors, and turbine blades in aeroengines.<sup>2–13</sup> One of the most widely used methods is cellular automaton–finite element (CAFE)<sup>14–16</sup> coupled with thermal models that solve the heat transfer during directional solidification. Despite the development of these models over the last two decades, there are significant practical challenges in using them for quantitative prediction due to the need to calibrate the nucleation parameters.

In the CAFE model, a Gaussian distribution of nucleation density as a function of the undercooling below the liquidus temperature is usually assumed

for equilibrium solidification processes. The maximum nucleation density, the corresponding mean nucleation undercooling, and its standard deviation are three parameters that determine the nucleation distribution. In previous studies, the effect of the nucleation parameters on the final grain structure were studied and their correlations to grain size were well understood. However, the selections of nucleation parameters for even identical nickel-based superalloys (such as the most studied CMSX-4) vary significantly. Both experimental measurements based on well-controlled thermal profiles and numerical investigation based on fitting microstructures have been used to generate such inputs. Bogner et al.<sup>17</sup> experimentally evaluated the undercoolings of different single-crystal Ni-based alloys, including CMSX-6 and two variants. Temperature measurements were conducted using the same thermal conditions in an Al<sub>2</sub>O<sub>3</sub>-SiO<sub>2</sub> investment casting shell mold system. The critical undercooling for nucleation ranged from 18°C to 100°C. Matache et al.<sup>8</sup> studied the effect of the surface nucleation

density (on the cooling plate) on the simulated grain structure of a single-crystal CMSX-4 casting and concluded, based on comparison with the grain size from experiments, that a value of  $10^7 \text{ m}^{-2}$  is optimal. Torroba et al.<sup>3</sup> calibrated the maximum nucleation density ( $5.5 \times 10^6 \text{ m}^{-2}$ ), mean nucleation undercooling ( $5.2^\circ\text{C}$ ), and its standard deviation ( $1.2^\circ\text{C}$ ) based on grain size measurements and visual comparison for a Mar-M247 superalloy casting of nozzle guide vanes. Li et al.<sup>18</sup> studied the effect of the mean nucleation undercooling ( $4.7\text{--}8.7^\circ\text{C}$ ) on the simulated grain structure of IN738LC casting and concluded that the determination of the mean nucleation undercooling is critical to predicting stray grain formation in the bulk and at certain special locations. Szeliga et al.<sup>7</sup> studied the effect of changing the maximum nucleation density ( $10^7 \text{ m}^{-2}\text{--}10^8 \text{ m}^{-2}$ ) and the standard deviation simultaneously on the grain structure of CMSX-4 directionally solidified castings, while keeping the mean nucleation undercooling constant at  $0.5^\circ\text{C}$ . Based on comparison with the predicted grain size and grain density, they concluded that the mean nucleation undercooling has the maximum effect on the grain structure and recommended the use of  $10^8 \text{ m}^{-2}$  as the maximum nucleation density and  $0.3^\circ\text{C}$  as the standard deviation. Rezaei et al.<sup>9</sup> selected a nucleation undercooling of  $7^\circ\text{C}$ , a deviation of  $1^\circ\text{C}$ , and a maximum nucleation density of  $10^7/\text{m}^{-3}$  for PWA 1483 nickel-based superalloy. In other studies,<sup>5-7,16-19</sup> a fixed set of nucleation parameters was used, some being based on indirect experimental measurements such as measurement of grain density using EBSD at locations close to the chill plate; For instance, Wang et al. reported the use of  $1.65 \times 10^8 \text{ m}^{-2}$  as the maximum nucleation density at the chill plate for DD403 superalloy casting based on EBSD measurements. Seo et al.<sup>6</sup> also adopted a similar approach and used a maximum nucleation density of  $8.39 \times 10^8 \text{ m}^{-2}$  for CMSX-4. However, the critical undercooling and standard deviation were not reported. Alloy composition may contribute to a range of nucleation parameters. Inconsistency of the values exists for the same alloy (i.e., CMSX-4) and similar casting processes in literature.<sup>21</sup> The determination of nucleation parameters remains an approximation of the actual solidification process. Therefore, calibration of the nucleation parameters is required to use the coupled thermal and CAFE model in quantitative grain structure prediction for any given alloy.

The calibration of a CA-based grain model and validation methods to quantitatively predict the grain structure of René N500 alloy with accuracy, which has not been studied in literature to the best of the authors' knowledge, are demonstrated herein. Using repeated experimental trials to account for process variability, the model is first applied to a simpler geometry of a step casting to calibrate the nucleation density by comparing the simulated

results with the experimentally determined grain size distribution. Using the calibrated model, the grain structure of a directionally solidified turbine blade is then simulated and compared with experimental results to validate the precalibrated nucleation parameters. The experiments performed in this study are described in "Experimental Procedures" section. A brief description of the models is provided in "Model Description" section, followed by the simulation setup and parameters. Finally, the results are presented and discussed in "Results and Discussion" section, along with a summary of the main findings of the study.

## EXPERIMENTAL PROCEDURES

Nickel-based René N500 superalloy with composition (wt.%) Ni-6Cr-6.5Al-7.5Co-1.5Mo-0.15Hf-6.6Ta-6.25W-0.04C-0.004B was used in this study. Two different directionally solidified casting geometries were used: a step casting ( $5.1 \text{ cm} \times 22.9 \text{ cm} \times 7.6 \text{ cm}$ ) and a turbine blade (of comparable size to the step casting), as shown in Fig. 1a and b with revealed grain structures. Note that a section of the turbine blade is blacked out due to its proprietary geometry design. Experiments were performed in an ALD Vacuum Technologies research casting furnace in vacuum with Bridgman mode. The mold heater set point was  $1550^\circ\text{C}$ . For step casting, a withdrawal speed of  $20.3 \text{ cm/h}$  was applied with three repeats to consider experimental variations. For turbine blades, two withdrawal speeds of  $10.2 \text{ cm/h}$  and  $20.3 \text{ cm/h}$  were applied to evaluate microstructure variations.

Figure 1c shows the furnace geometry for the step casting. To provide sufficient thermal data to validate the process model, eight type B Pt-Rh thermocouples (TC) were placed at various locations of the step casting (Fig. 1d). The TC positions were chosen to capture the temperature distribution influenced by the geometry asymmetry and cross section change of the step casting. All eight TCs (except TC4) were placed in the alloy at a distance of  $0.25 \text{ cm}$  from the alloy-shell interface to measure the evolution of the alloy temperature during the casting process. TC1, 2, 3, 6, and 7 were placed on the straight faces of the castings. TC4 was placed at the same height as TC3, but at the shell exterior surface to measure the shell temperature. TC5 was placed at the step face of the castings (opposite to the straight face). TC8 was placed at the side face. Similarly, for the blade casting with the  $10.2 \text{ cm/h}$  withdrawal speed, multiple thermocouples were placed in the alloy at a distance of  $0.25 \text{ cm}$  from the alloy-shell interface for temperature measurements (Fig. 1e). After casting and shell removal, the castings were macroetched using iron chloride etchant (in proportion  $80 \text{ ml HCl}$ ,  $2 \text{ ml HNO}_3$ ,  $11 \text{ ml H}_2\text{O}$ ,  $16 \text{ g FeCl}_3$ ) to reveal the grain structure. For each casting, transverse cross sections that solidified at sequential times were prepared

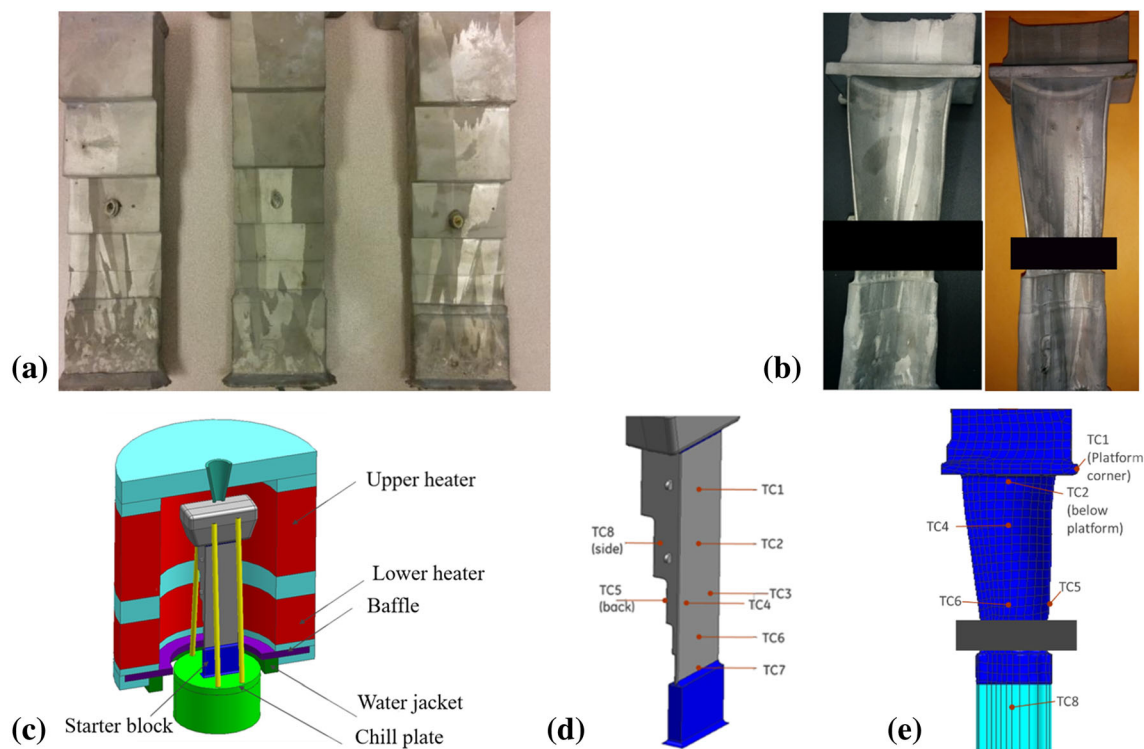


Fig. 1. Directionally solidified (a) step casting (three trials) and (b) turbine blade castings (10.2 cm/h withdrawal rate on the left and 20.3 cm/h on the right) used for calibrating and validating the models. (c) Furnace geometry for the step casting. (d) Locations of TC1 to 8 in the step casting, where the thermocouple measurements were made. (e) Locations of thermocouples in the blade casting

metallographically, etched using Stan's etchant, and characterized by light optical microscopy. Multiple areas of each single transverse cross section were examined at  $10\times$  magnification, which provides a resolution of 50 pixels per mm length. The sectional images were stitched together to show the grain structure of the entire cross section. Since the etchant revealed both grain boundary and dendrites, this also facilitated counting of grain numbers. Furthermore, to quantify the grain size distribution and grain orientations, EBSD was performed on selected sections using a JEOL 6610 SEM at accelerating voltage of 20 kV and step size of  $50\ \mu\text{m}$ . The selection of the step size was based on the primary dendritic arm spacing ranging from  $350\ \mu\text{m}$  to  $400\ \mu\text{m}$  at various sections under the withdrawal speed of  $20.3\ \text{cm/h}$ , which provides sufficient resolution to resolve all grains.

The following key material properties that were used as inputs for thermal models were measured experimentally up to the casting temperature: thermal conductivities, densities, and specific heats of the alloy, shell, and core (only for the blades). Density and thermal expansion were measured in accordance with ASTM E228 using a NETZSCH model DIL 402C pushrod dilatometer on cylindrical rod-shaped samples with diameter of 6.4 mm and length of 9 mm. Specific heat was measured according to ASTM E1269 using a NETZSCH model DSC 404 F1 Pegasus differential scanning calorimeter on

disc samples with diameter of 5.2 mm and thickness of 0.75 mm. Thermal diffusivity was measured by the flash method using a NETZSCH LFA 427 instrument on disc samples with diameter of 10.6 mm and thickness of 1.4 mm. The instrument and test method conform to ASTM E1461-01. Thermal conductivity was calculated as  $D = \lambda / C_p \rho$ , where  $D$  is thermal diffusivity,  $\lambda$  is thermal conductivity,  $C_p$  is specific heat, and  $\rho$  is density. Also, the latent heat and liquidus and solidus temperatures of the alloy were measured by differential scanning calorimetry (DSC; NETZSCH STA 449F5). René N500 has a solidus temperature of  $1330^\circ\text{C}$  and liquidus temperature of  $1383^\circ\text{C}$ . The measured cooling rates reported in "Model Description" section were calculated by linear fitting within the alloy solidification range. Due to proprietary constraints, the complete temperature-dependent materials properties are concealed in this paper.

## MODEL DESCRIPTION

A highly parallel solidification code was coupled with ESI's Casting Simulation suite, ProCAST, to predict the grain structure for as-cast parts. Within ProCAST, macroscale heat transfer equations are solved, taking into account the material's thermal properties, liquid-to-solid phase transformation, and latent heat released during solidification. The ray-tracing model provided in the software was applied for radiation. For the step casting, upper

and lower heaters (Fig. 1c) were assigned a fixed temperature of 1550°C, the water jacket was set at 300°C based on thermocouple data, while the chill plate was held constant at 20°C. The interface heat transfer coefficients (IHTCs) among the casting, chill plate, and shell were calibrated using thermocouple measurements of the furnace components. The IHTC between the casting and shell was temperature dependent: 200 W/m<sup>2</sup> K at 20°C, 250 W/m<sup>2</sup> K at 1000°C, and 950 W/m<sup>2</sup> K at 1600°C. The IHTC between the casting and chill plate was set constant as 200 W/m<sup>2</sup> K. An example of the predicted thermal contours is shown in Fig. 2a.

For the grain structure, a parallel solidification code, adapted from the open-source code  $\mu$ MaTIC,<sup>22–24</sup> was developed at GE Research. It uses the classic CAFE method as fully described in Ref. 14. In the mesoscale grain structure model, at every time step, the temperature profiles computed in ProCAST were taken as input for the CAFE model, thereby coupling the temperature evolution to grain growth. The parallel code takes a master–worker approach, where the master node allocates subdomains to each worker (computational node) for heavy computation based on the status of the thermal profiles; For instance, if the temperature in the subdomain is fully solid or below the solidus temperature, no calculation will be assigned to workers to reduce both calculation time and memory burden. This allows a significant increase of the computational efficiency for large and complex-geometry castings, using high-performance computing resources.

In the model, nucleation of new grains is modeled by assuming a Gaussian distribution of nucleation density ( $n$ ) with respect to undercooling ( $\Delta T$ ) below the liquidus temperature of the alloy:

$$\frac{dn}{d(\Delta T)} = \frac{n_{\max}}{\sqrt{2\pi}\sigma_n} \exp\left[-\frac{1}{2}\left(\frac{\Delta T - \Delta T_n}{\sigma_n}\right)^2\right],$$

where  $n_{\max}$  is the maximum nucleation density,  $\sigma_n$  is the standard deviation of the Gaussian distribution, and  $\Delta T_n$  is the mean nucleation undercooling.

The grain growth is then simulated based on the Kurz–Giovanola–Trivedi (KGT) model:<sup>25</sup>

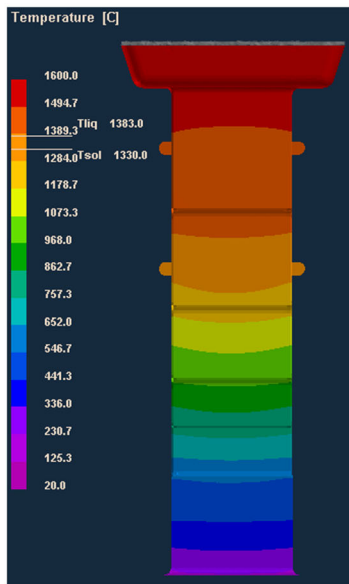
$$v = A(\Delta T)^2 + B(\Delta T)^3,$$

where  $v$  is the velocity of grain growth and  $A$  and  $B$  are growth coefficients.

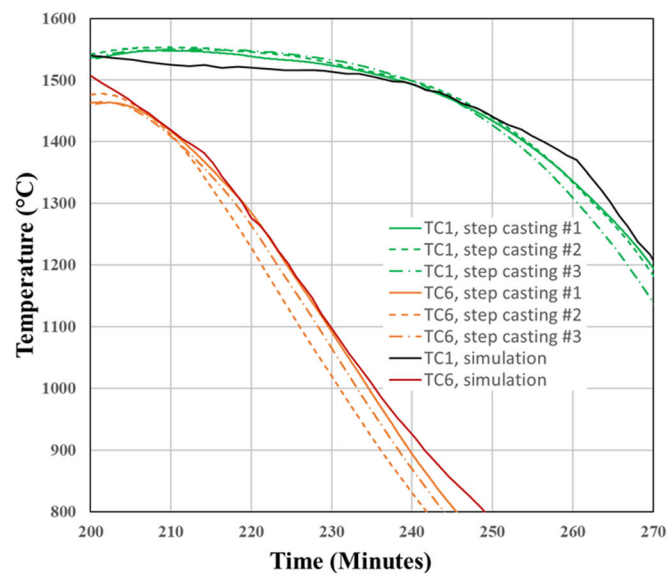
The solid fraction  $f_s$  is then obtained as

$$df_s = dt \times v.$$

The grain orientation is accounted for by using the decentered octahedron growth algorithm<sup>26,27</sup> to tackle anisotropy of the growth. Nucleation and grain growth parameters in the CAFE model were numerically determined through calibrations. Based on our previous experience with simulating single-crystal Ni-based superalloys in this composition range, the mean nucleation undercooling  $\Delta T_n$  was taken as 18°C with a standard deviation of 1°C for the René N500 alloy to restrict the bulk liquid nucleation. The maximum nucleation density  $n_{\max}$  was varied between  $5 \times 10^7 \text{ m}^{-3}$  and  $10^9 \text{ m}^{-3}$ . The coefficients in the KGT model were taken as



(a)



(b)

Fig. 2. (a) Predicted thermal profiles in ProCAST at 55 min after casting withdrawal. (b) Comparison of temperature profiles for thermocouples TC1 and TC6, located at the top and bottom of the step geometry, respectively

$A = 1 \times 10^{-6} \text{ m s}^{-1} \text{ K}^{-2}$  and  $B = 0 \text{ m s}^{-1} \text{ K}^{-3}$ . Nuclei with random orientations were initialized at temperatures low enough for nucleation to occur. The grid size used in the simulations was  $5 \times 10^{-4} \text{ m}$ , and the time step was  $1 \times 10^{-2} \text{ s}$ .

## RESULTS AND DISCUSSION

### Thermal Prediction for Step Geometry

The evolution of temperature for the step geometry was predicted by ProCAST. Figure 2a shows a snapshot of the temperature profile at 55 min after casting withdrawal. To evaluate the accuracy of the thermal model, the simulated temperatures at thermocouple locations were compared with experimental measurements. The temperature profiles for TC1 and 6 are shown in Fig. 2b. Table I presents a summary of the corresponding cooling rates at different locations.

The predictions show thermal profiles comparable to the measurements across all locations. Most of the predicted cooling rates match the values calculated from thermocouples with less than 12% deviation. Location 7 shows a larger deviation since it is very close to the chill and the heat transfer may not be captured accurately by the assumption of a constant chill plate temperature. Overall, there are good matches between the predicted temperatures from ProCAST and the measured temperatures from the thermocouples.

### Microstructures for Step Geometry

Interpolating the well-estimated temperatures, the grain structure model was first run for different maximum nucleation densities with a mean nucleation undercooling of  $18^\circ\text{C}$ . Note that the selection of  $18^\circ\text{C}$  was based on experiences with single-crystal Ni-based superalloys, which is also within the measured ranges from experiments.<sup>17</sup> Each simulation case is denoted as Nxx, where xx refers to the maximum nucleation density. Figure 3a shows the simulated structure with maximum nucleation density of  $1 \times 10^8 \text{ m}^{-3}$  (N1e8). The prediction qualitatively matches the grain structures shown in Fig. 1a. To perform a quantitative comparison, the

simulated grain structures were compared with the grain structures measured using EBSD at transverse sections of each step and the starter block. Figure 3b shows the inverse pole figure (IPF) map for each section. Figure 3b also shows the simulation results for N1e8 (center) and N1e9 (right). The number of grains was much higher with N1e9 than in the EBSD results, and the orientations also deviate much more. This is consistent with prior parametric studies on the effect of nucleation density.<sup>7,8</sup> The results from N1e8 are closest to the experimental measurements while considering the orientation.

Table II presents the grain density (number of grains/unit area) in the different transverse sections of the step casting measured by EBSD and calculated from the simulation results. With the increase in  $n_{\text{max}}$  from  $5 \times 10^7 \text{ m}^{-3}$  to  $10^9 \text{ m}^{-3}$ , the grain density in the starter block also increases, as expected. There is a steady decrease in the grain density from the starter block moving up to the fourth step. However, in the fifth step, there is a small increase in the grain density due to new nucleation. All simulations overestimate the grain density. Comparison with the starter block is generally not reliable, since there may be some transient growth behavior of the nuclei close to nucleation near the chill on the starter block, which is not well captured by the models. Although there is no perfect match, the results from N1e8 are overall closest to the experimental values, considering the grain number density together with the orientation maps. Therefore, the calibrated nucleation parameters from N1e8 from the step casting study are selected.

### Model Validation on Directionally Solidified Turbine Blades

Using the nucleation parameters calibrated from the step casting, we simulated the grain structure in the directionally solidified turbine blade shown in Fig. 1b for two different withdrawal rates.

Figure 4 shows the temperature profiles at different locations for the blade with a withdrawal rate of  $10.2 \text{ cm/h}$  measured from thermocouples and

**Table I. Cooling rates in  $^\circ\text{C}/\text{min}$  from thermocouple measurements at different locations shown in Fig. 1(d) of the step casting and the corresponding values from thermal simulations**

Thermocouple location	Cooling rate ( $^\circ\text{C}/\text{min}$ ) (measurement averaged over three castings)	Standard deviation of three castings	Cooling rate ( $^\circ\text{C}/\text{min}$ ) (simulation)	Difference (%)
1	11.9	<b>0.7</b>	11.9	0
2	12.8	<b>1.0</b>	12.1	5
3	12.9	<b>0.6</b>	13.4	- 4
4 (Shell)	15.8	<b>0.7</b>	13.8	12
5 (Back)	11.7	<b>0.8</b>	12.2	4
6	14.9	<b>2.7</b>	15.4	4
7	12.7	<b>0.8</b>	16.2	- 28
8 (Side)	13.7	<b>0.6</b>	12.7	7

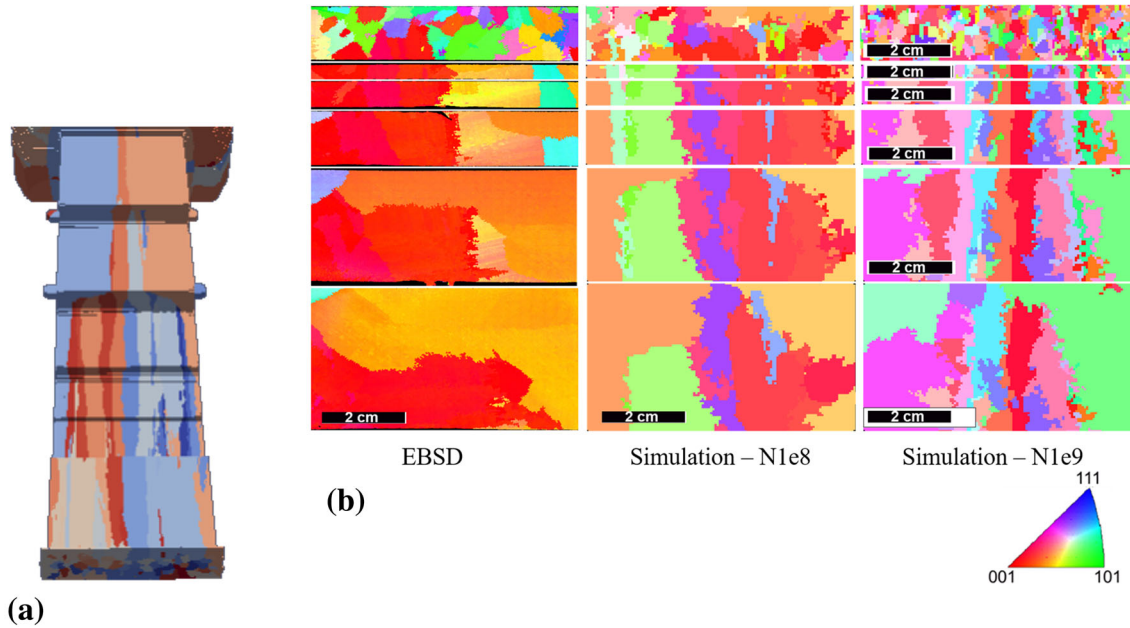


Fig. 3. (a) Predicted grain structure for step. (b) Transverse sections from the starter block, followed by the first, second, third, fourth, and fifth steps of the step casting. EBSD results of inverse pole figure map parallel to casting direction for the step geometry (left) and corresponding maps from simulations for maximum nucleation densities of  $10^8 \text{ m}^{-3}$  (N1e8, middle) and  $10^9 \text{ m}^{-3}$  (N1e9, right)

**Table II. Grain number/unit area ( $\text{cm}^{-2}$ ) of transverse sections of the step casting from EBSD and CAFE simulations with different maximum nucleation densities in the range from  $5 \times 10^7 \text{ m}^{-3}$  to  $10^9 \text{ m}^{-3}$  with mean nucleation undercooling of  $18^\circ\text{C}$**

Slice location	EBSD	N5e7	N1e8	N1e9
Starter block	9.9	6.5	11.6	40.3
First step	6.6	20.7	21.3	39.5
Second step	3.7	9.5	10.9	19.0
Third step	1.7	4.2	4.3	7.6
Fourth step	0.8	2.3	2.9	5.1
Fifth step	1.1	1.6	1.2	3.9

simulated using the thermal model. The model predicts the temperatures well for all locations except TC8, which shows some deviation due to its proximity to the starter block. This is similar to the step geometry, where a constant chill plate temperature was applied in the numerical model. In addition, the IHTCs were calibrated to ensure acceptable temperature profiles in the castings to better capture the grain structures. Similar accuracy was also achieved for the blade with withdrawal rate of  $20.3 \text{ cm/h}$ . Figure 5a shows an optical microscopy image of a selected area; both grain boundaries and dendrites can be observed. Figures 1b and 5b provide a visual comparison between the casting and the simulation of the overall grain structure for the blade with withdrawal rate  $20.3 \text{ cm/h}$ . The grain structures on five different transverse sections at different locations starting

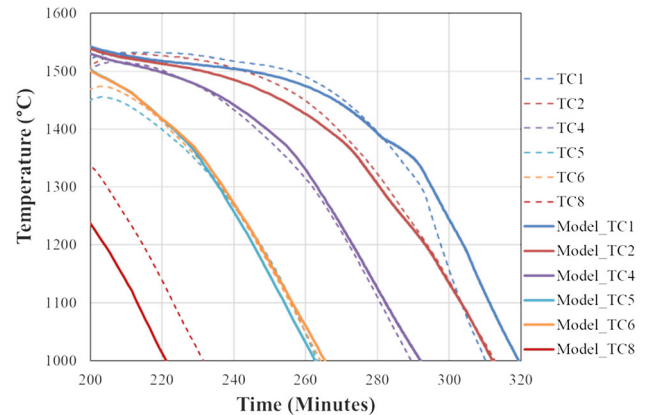


Fig. 4. Temperature profiles at different locations for blade with withdrawal rate of  $10.2 \text{ cm/h}$  compared with predictions from the thermal model

from the starter block up to the platform are shown in Fig. 5c. Slices 1, 2, 3, 4, and 5 were taken at the locations of TC8, TC6, TC4, TC2, and TC1 (the platform of the blade) as illustrated in Fig. 1e, respectively. The simulated structures show grains with different random orientations indicated by different colors. Table III(a) presents a comparison of the number of grains from the experiments and simulations. There is a good qualitative match between the actual and predicted structure. Note that the optical images captured at low magnification using a Keyence microscope in this study may underestimate the number of grains due to the similar light reflection properties for neighboring grains with similar misorientations. On the other

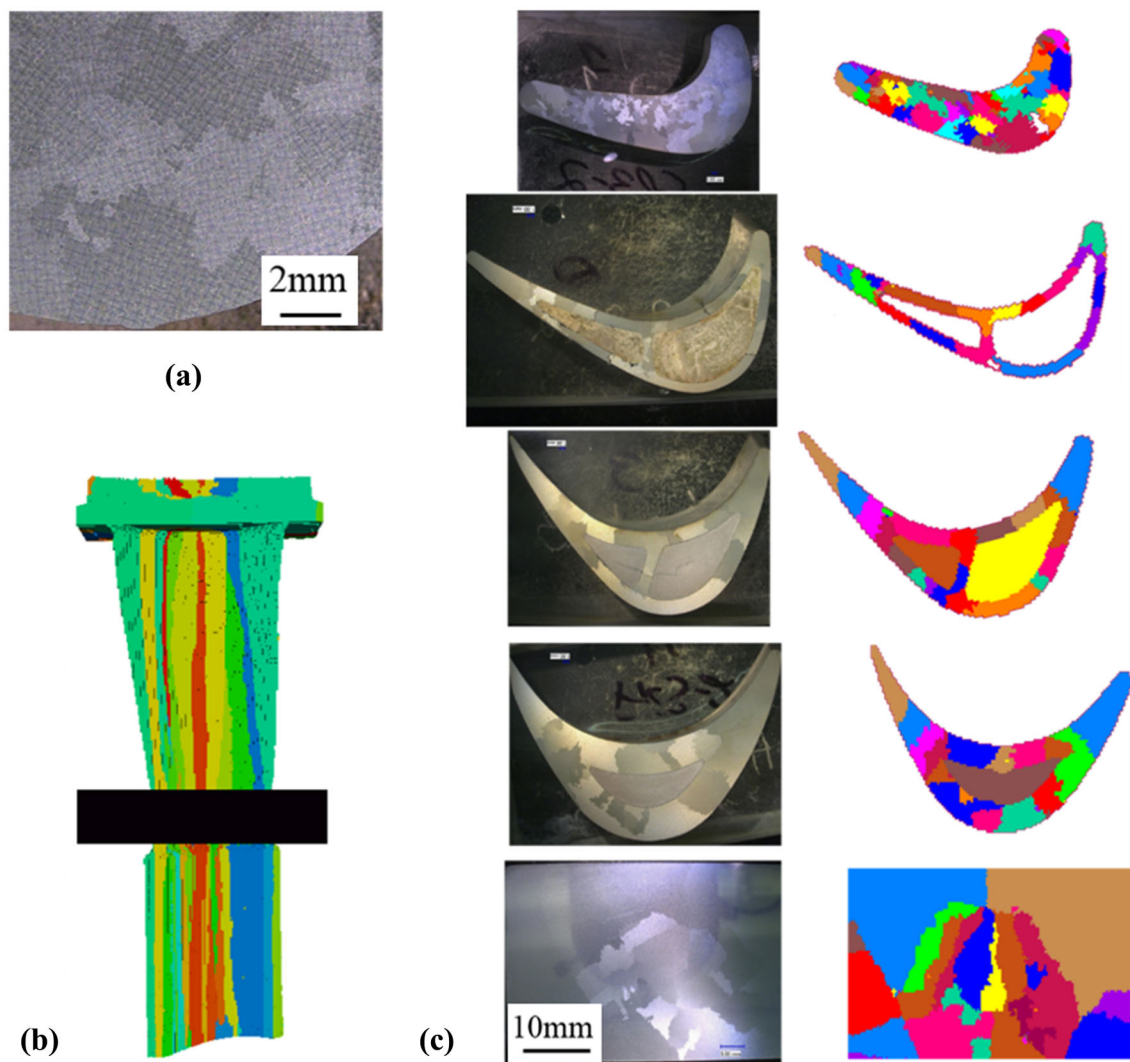


Fig. 5. (a) Optical image of a selected area on the blade with 20.3 cm/h withdrawal rate, showing both grain and dendritic structures, (b) Simulated blade with withdrawal rate of 20.3 cm/h, (c) corresponding grain structure on five transverse sections (slices 1–5 from top to bottom, corresponding to the end of the starter block to the platform, respectively) from simulations and optical micrographs. There is a good qualitative match between the simulated and the observed grain structure from optical micrographs. The different colors in the simulated structure refer to different random grain orientations (with no cut-off applied for low-angle grain boundaries)

hand, the nature of random nucleation leads to variations of grain numbers in the simulations. Therefore, to further confirm the predictions, EBSD was performed at four different transverse sections of the blade with withdrawal rate of 10.2 cm/h and compared with three repeats on the grain structure predictions.

Table III(b) presents the number of grains at the transverse sections from three different simulation runs and measurements from EBSD. Apart from slice 1, for which some deviation is expected due to the discrepancy on the thermal prediction as well as the different nucleation rate on the chill plate, the predictions for the other slices compare well with the measured grain numbers. There is a variation of up to 25% between the different simulation runs, which arises from the stochastic nature of random nucleation used in the model. Overall, the

predictions show results consistent with the experimental measurements.

With slower withdrawal rate, larger grain size is expected in comparison with faster withdrawal rate. With all confirmed experimental conditions, a smaller number of grains would be expected at the same location in the case of 10.2 cm/h than 20.3 cm/h. However, the simulation results presented in Table III show similar grain numbers for both cases. This suggests that the difference in withdrawal rate may not have been significant enough to cause a huge change in grain number. Moreover, the EBSD results show a significant decrease of grain number from 165 at slice 1 (54.1 mm from the chill plate) to 33 at slice 2 (106.2 mm from the chill plate). The change in grain numbers from the optical measurement is from 47 at slice 1 to 20 at slice 2. Both results confirm that the optical images

**Table III. Comparison of number of grains at different cross-sections of the blade between simulations and experimental measurements for withdrawal rate of (a) 20.3 cm/h and (b) 10.2 cm/h. N1e8 gives good match with experimental values**

Withdrawal rate, cm/h		Slice		Distance from Chill (mm)		Optical		N1e8	
(a)	20.3	1	54.1			47	86		
	20.3	2	106.2			20	27		
	20.3	3	146.8			16	23		
	20.3	4	170.4			18	22		
	20.3	5	186			23	3		
Withdrawal rate, cm/h		Slice		Distance from Chill (mm)		Optical		N1e8	
(b)	10.2	1	54.1	165	51	58	65		
	10.2	2	106.2	33	12	31	37		
	10.2	3	146.8	30	N/A	26	27		
	10.2	4	170.4	N/A	12	23	28		
	10.2	5	186	31	N/A	26	39		

obtained at low magnification in this study significantly underestimate the grain numbers.

The predicted number of grains close to the chill plate is consistently below the experimental measurements. This can be owing to a higher nucleation density rate on the cold surfaces. Since this study focuses on the bulk nucleation behavior of the single-crystal alloy, the effect of nucleation at the cold plate surfaces was ignored. Further improvements are required to take different nucleation rates at different surfaces into account. However, due to severe competition in the starting block, if there are a sufficient number of grains at the beginning with well-covered orientations, the grain structure predictions in the bulk materials remain valid. Only a limited number of grains with preferred orientations can survive and grow into the blade. The predictions for all the above cases also prove this.

The optimized set of parameters in this study lead to predictions within 25% of the measurements from EBSD for the blade casting when we consider the grain number. The results of this study show that the nucleation parameters can be calibrated with a simpler geometry and then used to study more complex geometries using the same setup. Given that several estimates in literature of the maximum nucleation density, mean nucleation undercooling, and standard deviation of nucleation undercooling can be applied to the same alloy or similar alloys, this provides a viable path that can aid in widespread adoption of thermal and grain structure models as design tools.

## CONCLUSION

The CAFE model parameters were calibrated and validated to simulate the grain structure of René N500 directionally solidified castings. Firstly, using a step casting with simpler geometry, the nucleation parameters used in the CAFE model were calibrated. The applicability of these parameters to simulate the grain structure of a directionally solidified turbine blade with much more complex geometry was then successfully demonstrated. The average grain numbers were predicted well for the step casting and the blade. This suggests that simpler geometries can be used for optimizing the parameters of the model using high-quality measurements of thermophysical properties of materials and EBSD maps of grain structures. The bulk nucleation parameters for René N500 cannot accurately capture the nucleation events on the chill plate, where numerous grains form. The predictions show that the severe competition of grain growth can mitigate this discrepancy and allow acceptable accuracy in the castings.

The coupled approach of a grain structure model and process model provides a viable path for optimization of directional solidification processes. Such application is particularly important for



single-crystal casting to minimize physical process iterations, achieve optimal casting conditions and geometry design, and avoid stray grain formation.

### ACKNOWLEDGEMENTS

The authors gratefully acknowledge technical support from Brian Ellis, Brody Smith, Jeremiah Faulkner, and Chris McLasky and valuable discussions with James Maughan, Christopher Hanslits, Mark Thompson, Judson Marte, Ade Makinde, and Michael Gigliotti.

### FUNDING

Funding was provided by General Electric.

### REFERENCES

- G.K. Bouse and J.R. Mihalisan, *Metallurgy of Investment Cast Superalloy Components* (New York: Academic Press, Inc., 1989).
- H.J. Dai, H.B. Dong, N. D'Souza, J.-C. Gebelin, and R.C. Reed, *Metall. Mater. Trans. A* 42, 3439 (2011).
- A.J. Torroba, O. Koeser, L. Calba, L. Maestro, E. Carreño-Morelli, M. Rahimian, S. Milenkovic, I. Sabirov, and J. LLorca, *Integr. Mater. Manuf. Innov.* 3, 369 (2014).
- Q. Xu, C. Yang, H. Zhang, X. Yan, N. Tang, and B. Liu, *Metals (Basel)* 8, 632 (2018).
- H.J. Dai, J.C. Gebelin, N. D'Souza, P.D. Brown, and H.B. Dong, *Int. J. Cast Met. Res.* 22, 54 (2009).
- S.M. Seo, I.S. Kim, J.H. Lee, C.Y. Jo, H. Miyahara, and K. Ogi, *Met. Mater. Int.* 15, 391 (2009).
- D. Szeliga, K. Kubiak, A. Burbelko, M. Motyka, and J. Sieniawski, *J. Mater. Eng. Perform.* 23, 1088 (2014).
- G. Matache, D.M. Stefanescu, C. Puscasu, E. Alexandrescu, and A. Bührig-Polaczek, *Int. J. Cast Met. Res.* 28, 323 (2015).
- M. Rezaei, A. Kermanpur, and F. Sadeghi, *J. Cryst. Growth* 485, 19 (2018).
- H.J. Dai, J.C. Gebelin, M. Newell, R.C. Reed, N. D'Souza, P.D. Brown, and H.B. Dong, in *Proceedings of the International Symposium Superalloys*, vol. 367 (2008).
- S.F. Gao, L. Liu, N. Wang, X.B. Zhao, J. Zhang, and H.Z. Fu, *Metall. Mater. Trans. A Phys. Metall. Mater. Sci.* 43, 3767 (2012).
- X. Meng, Q. Lu, J. Li, T. Jin, X. Sun, J. Zhang, Z. Chen, Y. Wang, and Z. Hu, *J. Mater. Sci. Technol.* 28, 214 (2012).
- D. Pan, Q. Xu, B. Liu, J. Li, H. Yuan, and H. Jin, *JOM* 62, 30 (2010).
- M. Rappaz and C.-A. Gandin, *Acta Metall. Mater.* 41, 345 (1993).
- M. Rappaz and C.A. Gandin, *MRS Bull.* 19, 20 (1994).
- C.A. Gandin, J.L. Desbiolles, M. Rappaz, and P. Thévoz, *Metall. Mater. Trans. A Phys. Metall. Mater. Sci.* 30, 3153 (1999).
- S. Bogner, E. Ivanova, M. Müller, F. Wang, D. Ma, and A. Bührig-Polaczek, *Metals* 5, 1971 (2015).
- X.-M. Li, J.-Y. Zhang, B. Wang, Z.-M. Ren, and G.-Z. Zhou, *J. Cent. South Univ. Technol.* 18, 23 (2011).
- P. Carter, D.C. Cox, C.A. Gandin, and R.C. Reed, *Mater. Sci. Eng. A* 280, 233 (2000).
- N. Wang, L. Liu, S. Gao, X. Zhao, T. Huang, J. Zhang, and H. Fu, *J. Alloys Compd.* 586, 220 (2014).
- A. Kermanpur, N. Varahram, P. Davami, and M. Rappaz, *Metall. Mater. Trans. B Process Metall. Mater. Process. Sci.* 31, 1293 (2000).
- L. Yuan and P.D. Lee, *Acta Mater.* 60, 4917 (2012).
- L. Yuan and P.D. Lee, *Model. Simul. Mater. Sci. Eng.* 18, 55008 (2010).
- W. Wang, P.D. Lee, and M. McLean, *Acta Mater.* 51, 2971 (2003).
- W. Kurz, B. Giovanola, and R. Trivedi, *Acta Metall.* 34, 823 (1986).
- C.-A. Gandin, R.J. Schaefer, and M. Rappax, *Acta Mater.* 44, 3339 (1996).
- C.-A. Gandin, M. Rappaz, and R. Tintillier, *Metall. Mater. Trans. A* 25, 629 (1994).

**Publisher's Note** Springer Nature remains neutral with regard to jurisdictional claims in published maps and institutional affiliations.